Supporting Information

Molecular linker engineering $CdS/Cu_2ZnSn(S,Se)_4$ interface for efficient photovoltaics

Yawei Wang[a], Lingling Wang*[a], Yinglin Wang[a], Hancheng Zhu[a], Zhengji Zhou[b], Sixin Wu*[b], Yichun Liu[a] and Xintong Zhang*[a]

[a] *State Key Laboratory of Integrated Optoelectronics, Key Laboratory of UV Light-Emitting Materials and Technology of Ministry of Education, Center for Advanced Optoelectronic Functional Materials Research, School of Physics, Northeast Normal University, Changchun 130024, Jilin, China*
[b] *Key Lab for Special Functional Materials Ministry of Education, National & Local Joint Engineering Research Center for High-Efficiency Display and Lighting Technology, School of Nanoscience and Materials Engineering, Henan University, Kaifeng 475004, Henan, China*

*Corresponding author.
E-mail address: wangll876@nenu.edu.cn (L.L. Wang); wusixin@henu.edu.cn (S.X. Wu); xtzhang@nenu.edu.cn (X.T. Zhang)

1. Experimental section

1.1. Materials

$Cu(AC)_2·H_2O$ (98+%, Alfa Aesar), CuCl (97%, Alfa Aesar), $SnCl_2·2H_2O$ (98.0-103.0%, Alfa Aesar), $SnCl_4·5H_2O$ (98%, Aladdin), $Zn(AC)_2·2H_2O$ (98.0-101.0%, Alfa Aesar), AgCl (99.5%, Aladdin), thiourea (TU, 99%, Alfa Aesar), 2-methoxyethanol (MOE, ≥ 99.7%, Macklin), $CdSO_4·8/3H_2O$ (99%, Aladdin), glycine (Gly, ≥ 99%, Aladdin), cysteine (Cys, 99%, Aladdin), lysine (Lys, 98%, Aladdin), aspartic acid (Asp, 98%, Aladdin), valine (Val, 98%, Energy Chemical), sarcosine (Sar, 98%, Energy Chemical), leucine (Leu, 99%, Aladdin), tyrosine (Tyr, 99%, Energy Chemical), citrulline (Cit, 99%, Energy Chemical), and methionine (Met, 99%, Aladdin) were used as received without further purification. Selenium particles (Se), ZnO, and ITO were obtained from ZhongNuo Advanced Material (Beijing) Technology Co., Ltd.

1.2. Preparation of the solutions

DMF system CZTSSe precursor solution (DMF-ps), 1.0095 g of $Cu(AC)_2·H_2O$, 0.7450 g of $SnCl_2·2H_2O$, 0.8518 g of $Zn(AC)_2·2H_2O$, 1.9640 g of TU, and 0.0545 g of AgCl were dissolved in 10 mL of DMF and stirred at 60°C for 2 h to obtain DMF-ps.

MOE system CZTSSe precursor solution (MOE-ps), 0.3992 g of CuCl, 0.8940 g of $SnCl_4·5H_2O$, 0.6585 g of $Zn(AC)_2·2H_2O$, and 1.5186 g of TU were dissolved in 10 mL of MOE and stirred at 60°C for 1 h. Then, 0.0242 g of AgCl was added under continuous stirring for 1 h to obtain MOE-ps.

CBD precursor solutions with CdS (CBD-ps), 0.1154 g of $CdSO4·8/3H_2O$ was added to 250 mL of ultrapure water and stirred until dissolved, then 40 mL of ammonia was added to obtain the CBD-ps.

S source solution, 1.7102 g of TU was added to 15 mL of ultrapure water and stirred until dissolved to obtain the S source solution.

1.3. Fabrication of CZTSSe films and solar cells

Fabrication of absorber films:

DMF (MOE)-ps was spin-coated on molybdenum-coated soda-lime glass substrates at 3000 (2800) rpm for 30 (28) s and annealed at 300 (280) °C for 2 min on a hot plate. This procedure was repeated 8 (12) times to receive DMF (MOE)- CZTS

films with a thickness of approximately 2 μm. Subsequently, the DMF (MOE)-CZTS films were selenized at 580°C (560°C) for 1800 s (1100 s) in a graphite box with 0.80g of Se under N_2 atmosphere using a rapid thermal processing (RTP) furnace (MIT, OTF-1200X-4-RTP) to obtain the DMF (MOE)-CZTSSe absorber films.

Amino acid surface treatment:

All of Amino acid were prepared at a concentration of 1 mmol/L. The CZTSSe absorber films were immersed in amino acid solutions at 40°C for 1 minute, then rinsed with ultrapure water and dried under a nitrogen stream.

Fabrication of CZTSSe solar cells:

The treated and untreated CZTSSe absorber layer films were immersed in a 30°C CBD-ps solution for 3 min. Then, 15 mL of S-source solution was added, which was transferred to a 65°C water bath for CdS deposition to obtain the CdS/CZTSSe heterojunction films. Subsequently, ZnO (50 nm) and ITO (170 nm) layers were sequentially deposited onto the CdS surface by magnetron sputtering. Ag electrodes were also deposited onto the ITO surface by thermal evaporation. Finally, an MgF_2 anti-reflective coating was deposited onto the CZTSSe solar cell surface using the same thermal evaporation technique.

1.4. Theoretical calculation methods

Spin-polarized density functional theory DFT calculations were performed using the Vienna Ab Initio Simulation Package with projector augmented wave method. The exchange-correlation functional was treated within the generalized gradient approximation with Perdew-Burke-Ernzerhof parametrization. The energy cutoff for the plane wave basis set was set to 450 eV. Partial occupancies of the Kohn-Sham orbitals were allowed using the Gaussian smearing method with a width of 0.01 eV. The Brillouin zone was sampled with a Monkhorst mesh of 2 × 2 × 1 for optimization of all of the structures. The self-consistent field calculations employed a convergence energy threshold of 10^{-5} eV, and the force convergence was set to 0.05 eV/Å.

1.5. Characterization

Contact angle values of water and CBD-PS on different samples were measured by a droplet shape analyzer (KRUSS Scientific, DSA100, Germany). Fourier-transform

infrared (FTIR) spectra were collected using a Nicolet iS10 spectrometer (Thermo Fisher Scientific, USA). Energy-dispersive spectroscopy was performed using a Nanoanalysis Xplore30 instrument. Meanwhile, the photoluminescence (PL) spectrum and time-resolved photoluminescence (TRPL) spectra were recorded using a fluorospectrophotometer (Horiba Scientific, QuantaMaster 8000, USA). The PL excitation source consisted of a 450 nm laser (10 mW, about 1.80 mm^2, 0.56 W/cm^2), and the TRPL excitation source was a 635 nm NanoLED (Pulse Duration < 200 ps, 18 pJ/pulse). The average carrier lifetime was obtained by fitting with a Gaussian decay function (ExpDecay2). X-ray photoelectron spectroscopy (XPS) measurements were performed using a Shimadzu AXIS SUPRA+ spectrometer. All spectra were acquired under ultrahigh vacuum conditions using a monochromatic Al Kα (hν = 1486.6 eV) X-ray source. The binding energies were calibrated against the C 1s peak at 284.8 eV. Ultraviolet photoelectron spectroscopy (UPS) was measured using an X-ray photoelectron spectrometer (Shimadzu/Kratos, AXIS SUPRA+, Japan) with an He-I source (21.22 eV). The surface morphology of the CdS was measured using field emission scanning electron microscopy (Zeiss, Gemini Sigma 300, Germany). The cross-section SEM images of CZTSSe with different CdS deposition times were obtained by an FEI Quanta 250 scanning electron microscope system. AFM, KPFM, and C-AFM images were obtained using a Bruker Dimension Icon ScanAsyst system. *J–V* curves and maximum power point tracking (MPPT) measurements were carried out using an Enlitech AAA solar simulator (SS-F5-3A, Taiwan) at room temperature, in combination with a Keithley 2634 digital source meter for current–voltage acquisition. The intensity of the solar simulator was calibrated to 100 mW/cm^2 (AM 1.5 G) by a standard silicon cell with NIM305#. The external quantum efficiency (EQE) measurements were performed utilizing a Zolix SCS100 QE system.

2. Figures and tables

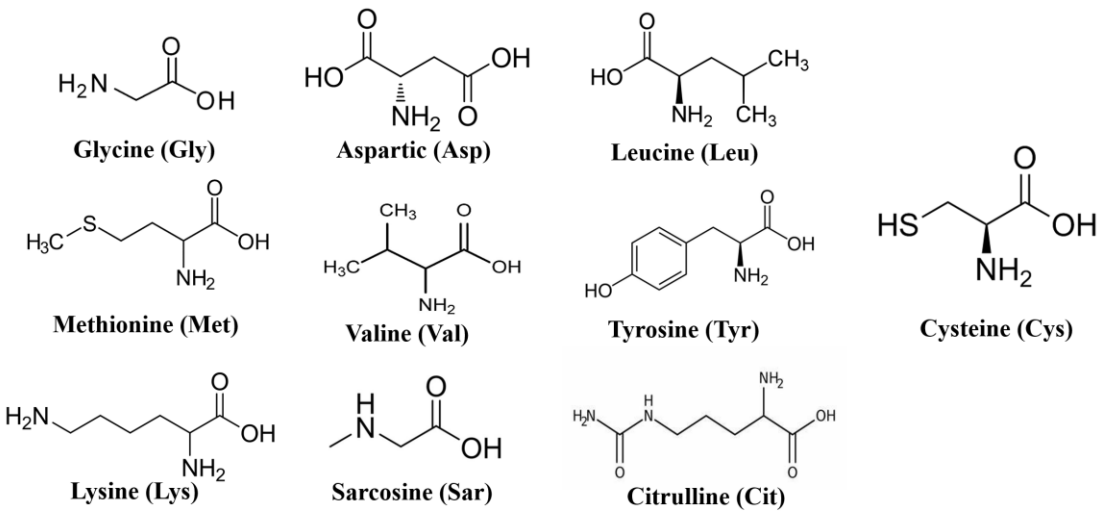

Fig. S1. Molecular structures of the 10 amino acid linker candidates selected in this study, namely, Gly, Lys, Asp, Val, Sar, Leu, Tyr, Met, Cys, and Cit. Among these, cysteine (Cys) demonstrated the most effective linker functionality in regulating CdS nucleation and passivating surface defects.

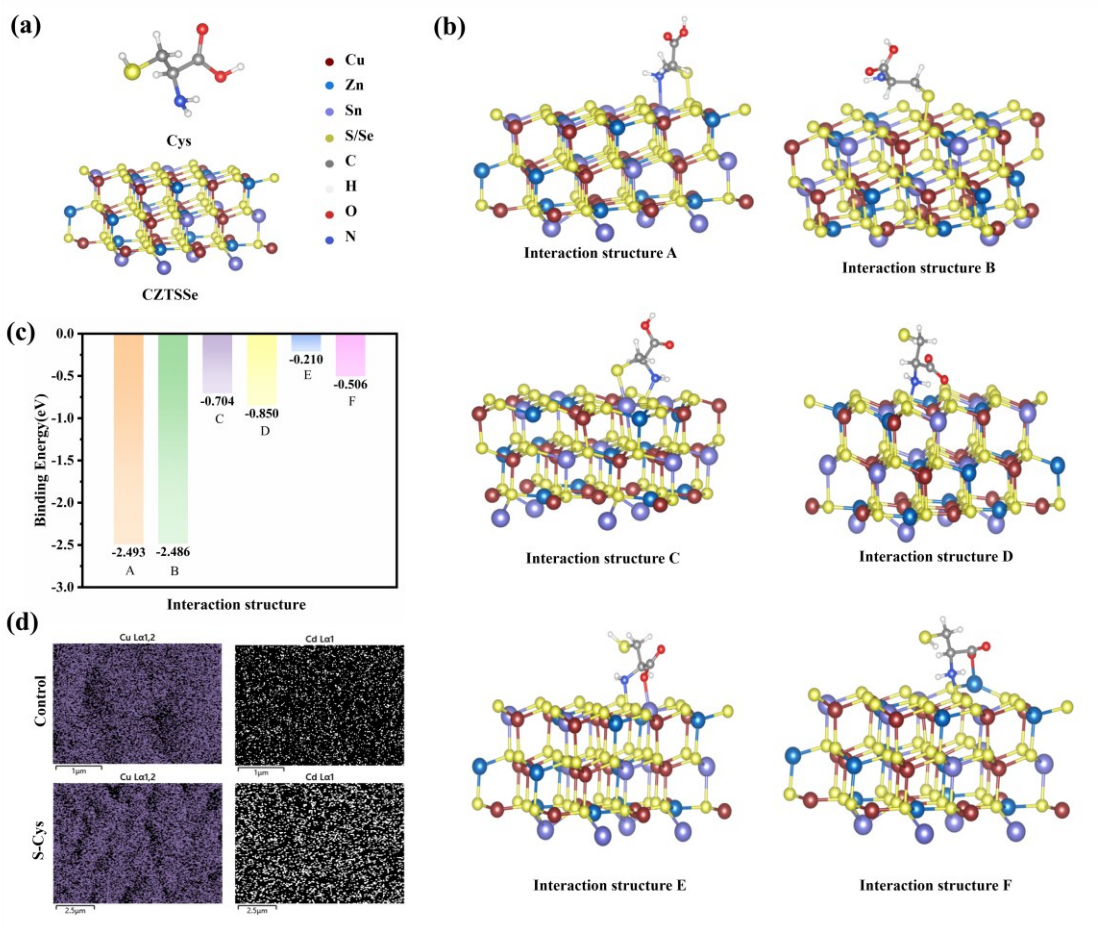

Fig. S2. (a) Schematic illustration of the molecular structure of cysteine and crystal lattice structure of CZTSSe; (b) stable interaction structures between the Cys molecules and CZTSSe (112) surface, as revealed by density functional theory (DFT) calculations; (c) calculated binding energies corresponding to stable interaction structures between cysteine and CZTSSe (112) surface; (d) elemental distribution maps of Cu and Cd on the surfaces of the untreated (Control) and Cys-treated (S-Cys) CZTSSe samples.

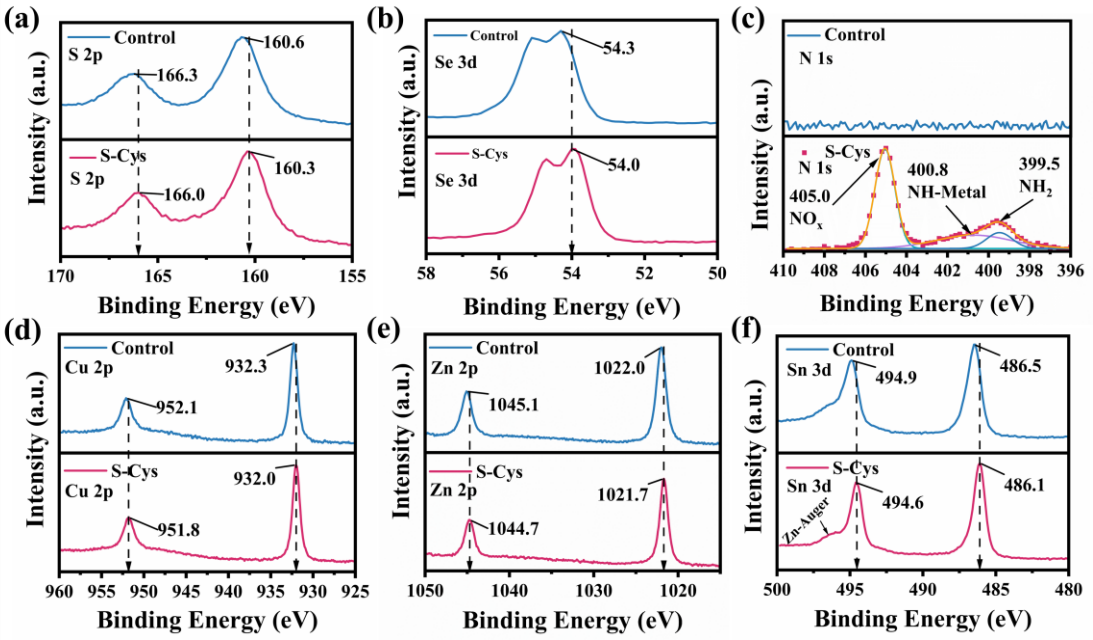

Fig. S3. XPS spectra of CZTSSe with and without Cys treatment. (a) S 2p, (b) Se 3d, (c) N 1s.(d) Cu 2p, (e) Zn 2p, (f) Sn 3d.

XPS measurements were performed on the CZTSSe surface before (Control) and after Cys treatment (S-Cys). In the CZTSSe structure (**Fig. S2a**), copper vacancies (V_{Cu}) can generate undercoordinated surface S atoms, and passivation of these vacancies requires elimination of such unsaturated S. After Cys treatment, a redshift in the S binding energy was observed without the appearance of new S peaks, likely due to interactions between the thiol (-SH) group of Cys and surface S atoms.[4] This observation is consistent with theoretical calculations and the PL-observed quenching of the V_{Cu} related Secondary fitting peak 2.

New N 1s signals appeared after Cys treatment. Besides the intrinsic $–NH_2$ peak of Cys, an additional peak corresponding to NH–Metal species emerged.[5,6] Meanwhile, Cu, Zn, and Sn core-level peaks shifted to lower binding energies, suggesting interactions between $–NH_2$ groups and surface metal atoms. This is also in agreement with the redshift of Secondary fitting peak 1 in the PL spectra. A peak corresponding to a higher oxidation state of nitrogen was also detected, which is likely from unbound $–NH_2$ groups partially oxidized in air. The possibility of N–Metal bonding contributing to this peak cannot be completely excluded.

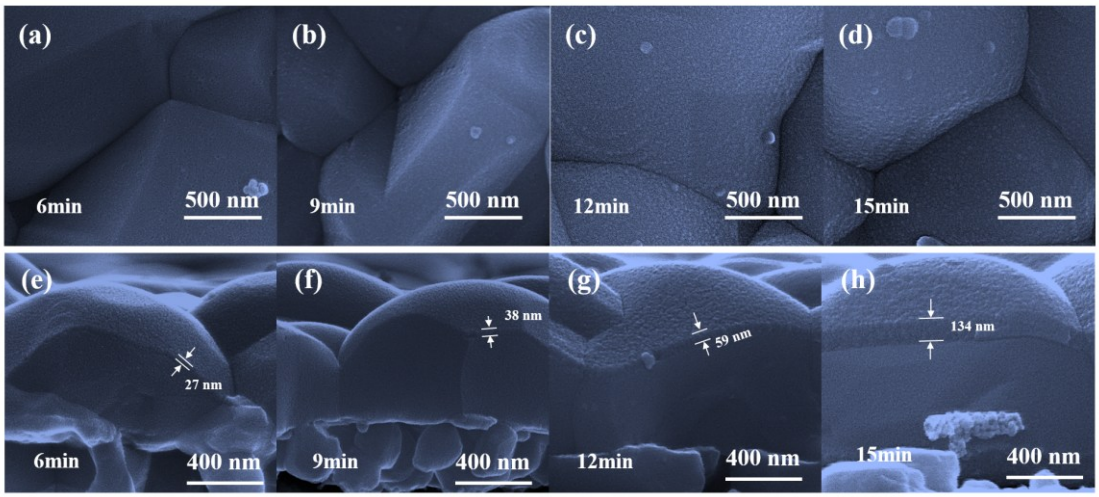

Fig. S4. (a–d) Top-view SEM images and (e–h) cross-sectional SEM images of the Control samples with CdS deposition times of 6, 9, 12, and 15 min. The control surfaces showed an evolution from porous morphology to partial film formation with increasing deposition time.

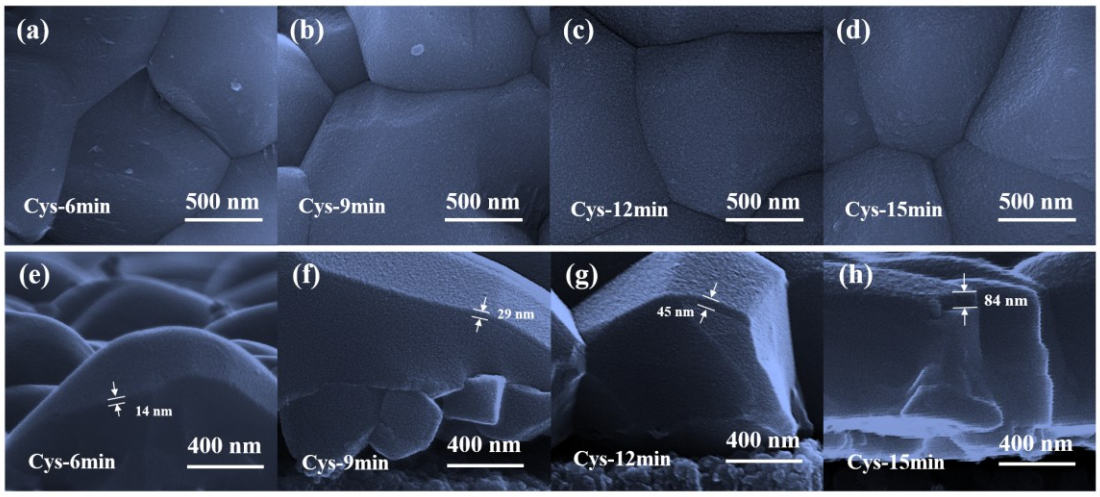

Fig. S5. (a–d) Top-view SEM images and (e–h) cross-sectional SEM images of the S-Cys samples with CdS deposition times of 6, 9, 12, and 15 min. The S-Cys surfaces exhibited uniform and compact CdS growth from the early stages, with no visible voids throughout the deposition process.

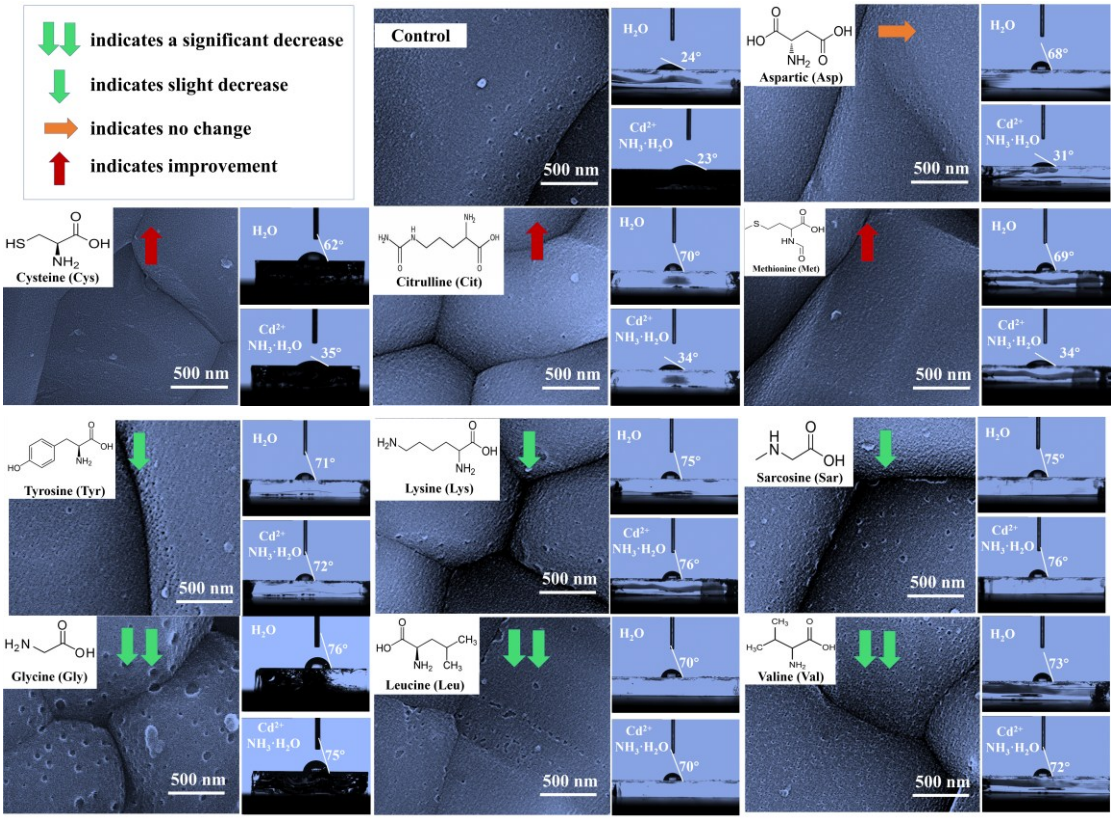

Fig. S6. SEM images of CdS films deposited for 6 min after treatment with different amino acids, including molecular structures (top left), corresponding device efficiencies (indicated by arrows), and contact angles (right).

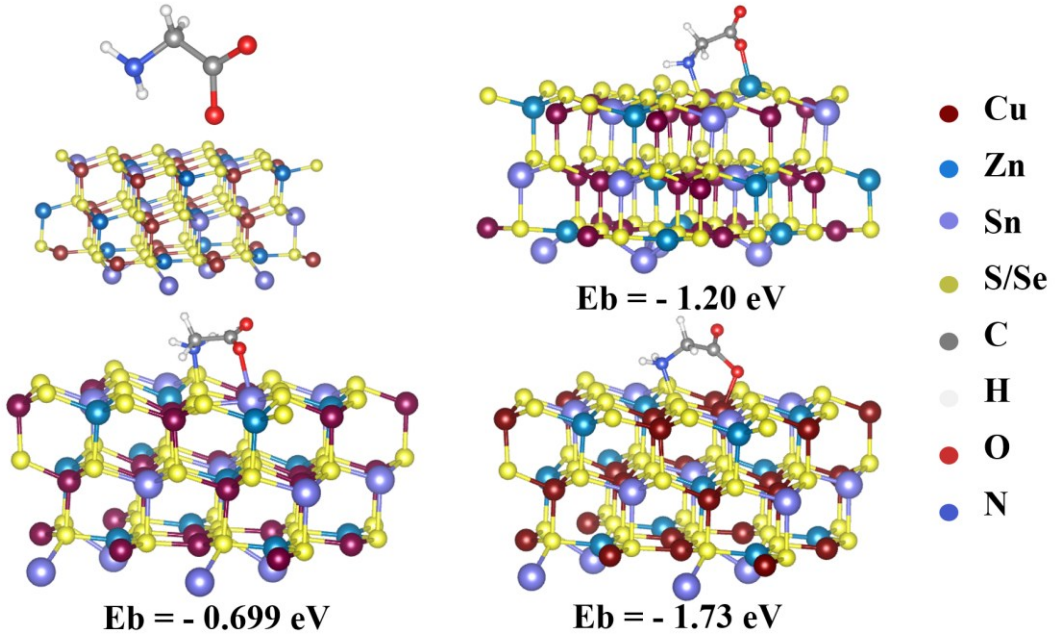

Fig. S7. Stable interaction structures between the Gly molecules and CZTSSe (112) surface, as revealed by density functional theory (DFT) calculations, along with their corresponding binding energies (Eb).s

To more clearly elucidate the correlation between molecular structures and device performance, we systematically summarized the molecular structures, device efficiencies, contact angles (water and $NH_3 \cdot H_2O$ & Cd^{2+} solutions) before and after molecular treatment, as well as the CdS surface morphology after 6 min of deposition (**Fig. S6**). Our intention was to establish more instructive relationships between molecular structure and device behavior to guide future molecular design. However, in such a complex chemical system with strongly coupled factors, our current analytical capability remains limited, making it challenging to derive a highly generalized and universally applicable correlation. Nevertheless, we believe that the three molecule-selection principles proposed in the main manuscript remain well-founded and representative. Based on a further analysis of **Fig. S6**, we refined and supplemented these principles as detailed below.

First, to obtain a more intuitive understanding of the underlying mechanism, we performed DFT calculations on Gly, which yields the poorest device performance **(Fig. S7**). The results show that both the amino and carboxyl groups of Gly can interact with the CZTSSe surface, and the molecule tends to anchor through simultaneous adsorption of both groups. This dual-site anchoring leaves almost no outward-exposed functional groups available for $[Cd(NH_3)_4]^{2+}$ coordination, a finding consistent with the hydrophobic contact angle observed in the $NH_3 \cdot H_2O$ & Cd^{2+} solution. The lack of external $[Cd(NH_3)_4]^{2+}$ binding sites hinders uniform CdS nucleation, resulting in pronounced pinholes in SEM images and, consequently, degraded device performance. For Leu and Val molecules, the CdS morphology closely resembles that of Gly, and the device efficiencies also decrease markedly. Although their additional $–CH_2–$ groups make them structurally larger, these groups do not provide effective sites for Cd^{2+} binding, and thus fail to improve CdS nucleation.

For Tyr, Lys, and Sar molecules—whose device performance decreases only slightly—the CdS uniformity is significantly improved compared with Gly. Structural comparison shows that these molecules either contain more types of functional groups (e.g., –OH, –NH–) or a higher number of groups (e.g., additional $–NH_2$). These additional functionalities enhance molecular anchoring and increase the availability of

Cd^{2+} adsorption sites, demonstrating the potential advantages of multi-functional-group molecules.

For Asp molecules, which yields nearly unchanged device performance, the CdS film remains uniform and compact with no visible pinholes. Compared with Gly, Asp contains one additional carboxyl group, which appears to provide a positive effect. Interestingly, although Lys also contains one additional amino group relative to Gly, its device performance decreases, suggesting that in this system the carboxyl group is more effective than the amino group in enhancing $[Cd(NH_3)_4]^{2+}$ interfacial adsorption.

For Cys, Cit, and Met molecules —which lead to significant performance enhancement—the CdS morphology becomes even more uniform and refined. Although the specific mechanism responsible for the behavior of Cit remains difficult to fully resolve at this stage, the results for Cys and Met clearly highlight the critical role of sulfur-containing groups. Since thiol, amino, and carboxyl groups can all interact with the CZTSSe surface—while –SH typically shows the strongest anchoring tendency when multiple groups coexist—competitive interactions among these groups should be carefully considered in future molecular design.

Based on the above analysis, we provide the following refined principles to complement the original selection criteria:

Original selection criteria:

(1) Molecules should contain multiple functional sites capable of interacting with both the CZTSSe surface and the $[Cd(NH_3)_4]^{2+}$ intermediates during CdS CBD.

(2) The functional groups responsible for CZTSSe anchoring and those responsible for $[Cd(NH_3)_4]^{2+}$ coordination should each possess clear selectivity.

(3) The molecular chain length should be minimized to avoid hindering carrier transport across the heterojunction interface.

Additional principles:

(4) **Functional groups within a molecule should exhibit sufficiently different interaction strengths with the CZTSSe surface**, ensuring that after effective interfacial anchoring, at least one group remains outward-exposed to bind $[Cd(NH_3)_4]^{2+}$ and promote uniform CdS nucleation.

(5) **Increasing the number of functional groups can be beneficial**, as it enhances both the anchoring stability on the CZTSSe surface and the molecule's ability to coordinate $[Cd(NH_3)_4]^{2+}$, thereby facilitating the formation of a uniform and compact CdS layer.

We believe that these additional analyses further reinforce the selection principles proposed in the manuscript and provide useful guidance for the rational design of interface-modifying molecules for future studies

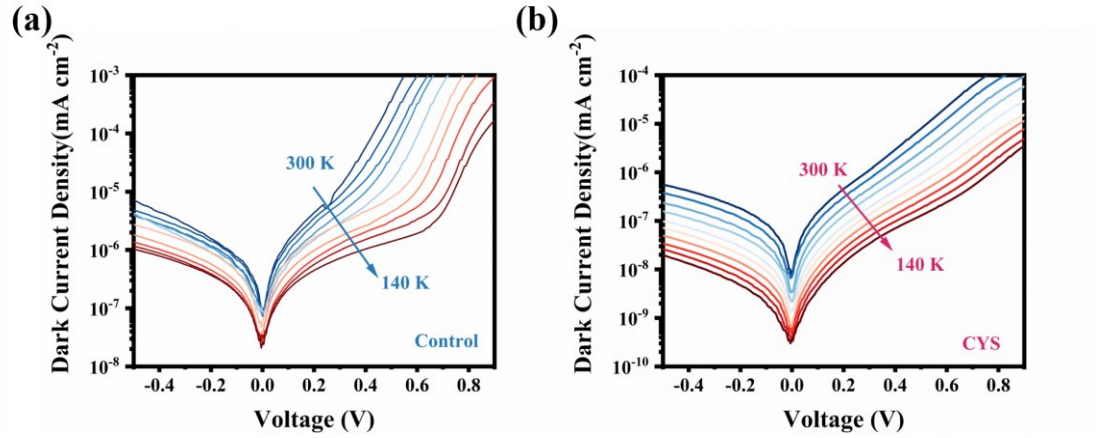

Fig. S8. Temperature-dependent dark *J-V* curves of Control (a) and CYS (b) devices.

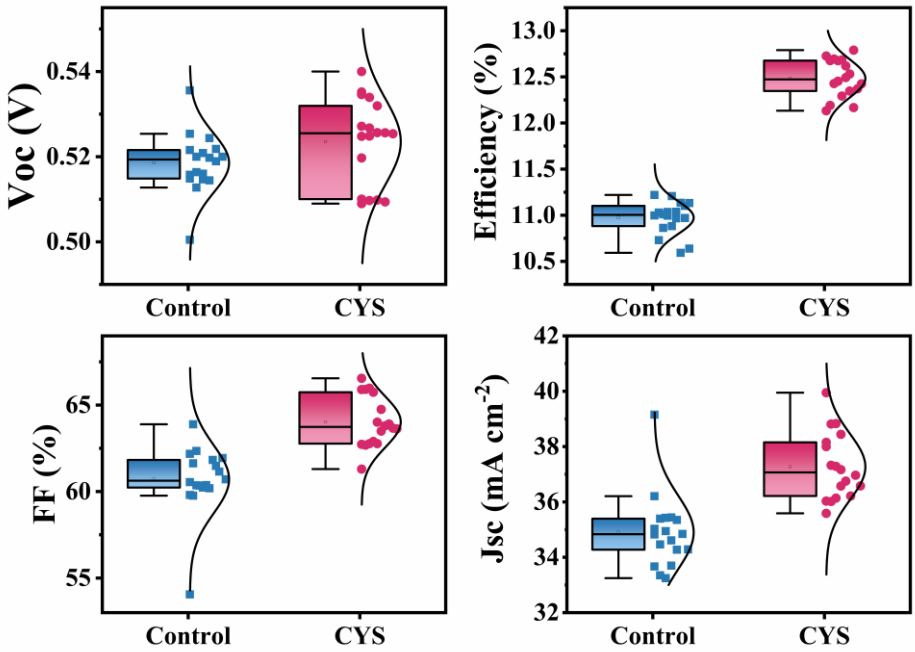

Fig. S9. Statistical distribution of device performance parameters for CYS and the Control device (MOE solution preparation).

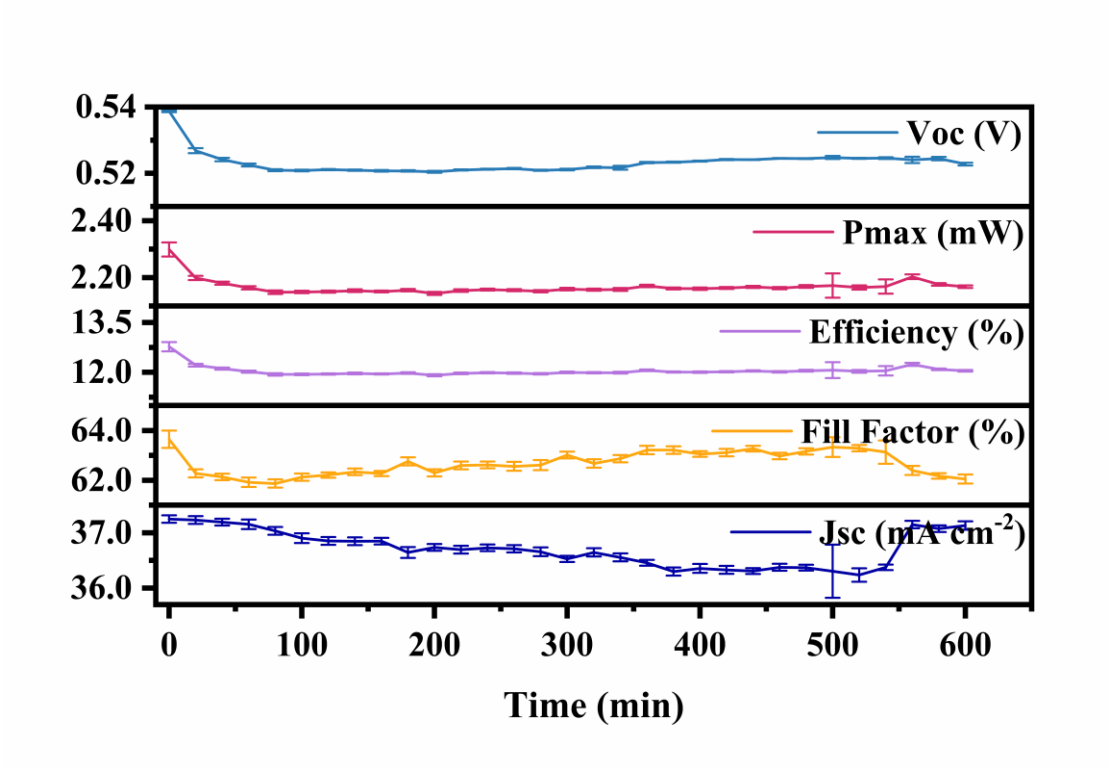

Fig. S10. Stability of the devices prepared in the MOE solution system after introducing Cys, tested in air under 1 sun illumination.

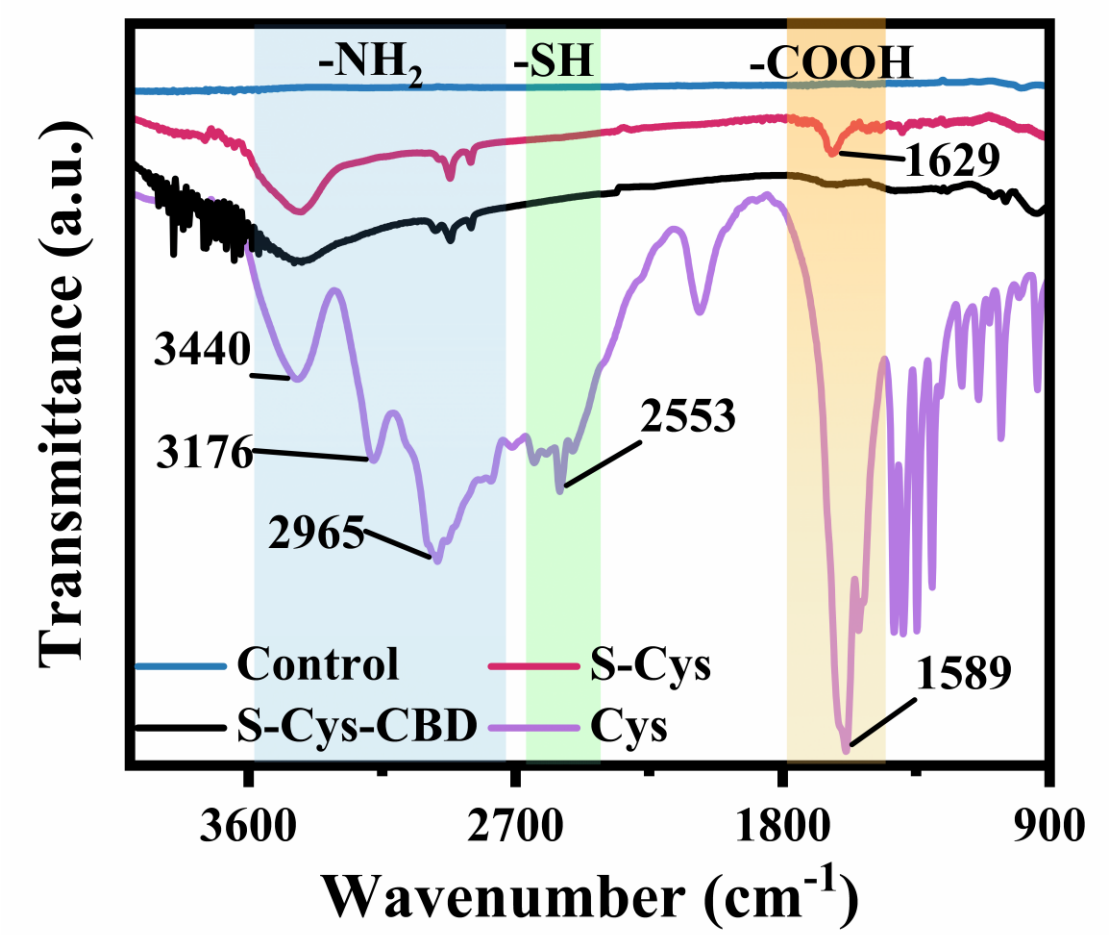

Fig. S11. FTIR spectra of bare CZTSSe film (Control), Cys-treated film (S-Cys), Cys-treated film after exposure to an $NH_3 \cdot H_2O$ & Cd^{2+} solution at 65 °C for 15 minutes (S-Cys-CBD), and pure Cys powder.

The chemical stability of Cys during the CBD process was investigated using FTIR spectroscopy (**Fig. S11**). Spectra were recorded for the bare CZTSSe film (Control), Cys-treated film (S-Cys), Cys-treated film after exposure to $NH_3 \cdot H_2O$ & Cd^{2+} solution at 65 °C for 6 min (S-Cys-CBD), and pure Cys powder. Compared with the Control, the S-Cys film showed characteristic Cys features in the $–NH_2$ (2700–3600 cm^{-1}) and –COOH (1400–1800 cm^{-1}) regions,[1,2] while no new peak appeared near 2550 cm^{-1} (–SH), indicating that the thiol groups of Cys formed strong interactions with the CZTSSe surface.[3] After CBD treatment, $–NH_2$ bands remained visible, whereas –COOH bands weakened, suggesting that Cys remains stably adsorbed on CZTSSe under alkaline CBD conditions, with partial –COOH involvement in Cd^{2+} coordination.

Table S1. Atomic concentrations (at.%) of Cu and Cd in Control and S-Cys CZTSSe samples after 3 min immersion in $[Cd(NH_3)_4]^{2+}$ solution, as determined by EDX.

Samples	Cd (At%)	Cu (At%)	Cd/Cu	Average	Variance
Control	0.20	20.30	0.00985	0.00817	0.00231
	0.20	20.50	0.00976		
	0.10	20.40	0.00490		
S-Cys	0.45	17.33	0.02597	0.02542	0.00064
	0.50	19.40	0.02577		
	0.43	17.54	0.02452		

Table S2. Cd and Cu atomic contents on the surfaces of the Control samples with different CdS deposition times.

Times (s)	Cd (At%)	Cu (At%)	Cd/Cu	Average	Variance
6	1.10	17.96	0.061	0.06073	0.00037
	1.07	17.71	0.060		
	1.06	17.51	0.061		
9	1.40	17.55	0.080	0.07983	0.00182
	1.43	17.42	0.082		
	1.36	17.52	0.078		
12	2.72	17.79	0.153	0.14775	0.00697
	2.46	17.84	0.138		
	2.72	17.84	0.152		
15	5.01	16.49	0.304	0.30976	0.00441
	5.12	16.46	0.311		
	5.09	16.19	0.314		

Table S3. Cd and Cu atomic contents on the surfaces of the S-Cys samples with different CdS deposition times.

Times (s)	Cd (At%)	Cu (At%)	Cd/Cu	Average	Variance
	1.00	**17.68**	**0.057**		
6	**1.01**	**17.89**	**0.056**	**0.05699**	**0.00068**
	1.04	**17.95**	**0.058**		
	1.47	**17.45**	**0.084**		
9	**1.48**	**18.11**	**0.082**	**0.08260**	**0.00116**
	1.46	**17.84**	**0.082**		
	2.57	**17.45**	**0.147**		
12	**2.53**	**17.64**	**0.143**	**0.14463**	**0.00188**
	2.52	**17.60**	**0.143**		
	4.30	**16.54**	**0.600**		
15	**4.25**	**16.73**	**0.254**	**0.25953**	**0.00431**
	4.72	**17.84**	**0.265**		

3. Supplementary Notes:

3.1 Details of UPS analysis

UPS spectra of the CZTSSe and Cys-treated CZTSSe samples measured using He I (hν = 21.22 eV) excitation. A −5 V sample bias was applied to clearly resolve the secondary electron cutoff (SECO), and all cutoff energies were corrected for this bias. The SECO edge was obtained by linear extrapolation of the rising intensity to the baseline (Fig. 2d left, Control: 17.09 eV and S-Cys: 16.60 eV) and the energy offset between the valence band maximum (VBM) and the Fermi level (BE_{VBM}) was determined by linear fitting of the leading edge (Fig.2d right, Control: 0.28 eV and S-Cys: 0.33 eV).

3.2 Calculation of E_f, VBM, and CBM

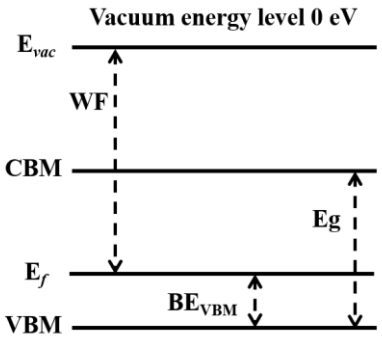

The Fermi level (E_f) can be determined from the following equation:

$$E_{vac} - E_f = \mathrm{WF} = h\nu - E_{SECO}$$

$$E_{vac} = 0 \text{ eV}$$

$$E_f = -\mathrm{WF} = E_{SECO} - h\nu$$

The energy level of VBM (E_v)can be determined from the following equation:

$$BE_{VBM} = E_f - E_v$$

$$E_v = E_f - BE_{VBM}$$

The energy level of conduction band minimum (CBM) (E_c) can be determined from the following equation:

$$E_c = E_v + \mathrm{Eg}$$

The energy bandgap (Eg) can be determined from the photoluminescence (PL) spectras.

References

1. Q. Guo, X. Ma, Y. Xie, W. Tan, H. Zhang, Green synthesis and formation mechanism of Ag nanoflowers using l-cysteine and the assessment of Ag nanoflowers as SERS substrates, Colloids and Surfaces A: Physicochemical and Engineering Aspects, 2017, **530**, 33-37
2. X. Du, M. Li, M. Du, A. Shen, X. Hao, J. Yuan, S. Ma, Y. Zhao, L. Hou, Z. Lia, Y. Yang, A one-pot strategic construction of functionalized nanomaterial ZIF-90-Rhn for stepwise detection and capturing of Ag^{+} and formaldehyde from an aqueous solution, Mater. Adv., 2022, **3**, 3457-3468.
3. L. Gao, X. Hu, S. Qin, H. Chu, X. Zhao, B. Wang, l-Cysteine modified metal–organic framework as a chiral stationary phase for enantioseparation by capillary electrochromatography, RSC Adv., 2022, **12**, 6063-6075.
4. Y. Wang, J. Guo, L. Siqin, C. Yang, L., S. Li, R. Liu, H. Luan, C. Zhu, Enhancing the photovoltaic efficiency of CZTSSe thin-film solar cells via Ag-doping induced defect modulation, Solar Energy Materials and Solar Cells, 2024, **277**, 113138.
5. C. Xie, L. Lin, L. Huang, Z.Wang, Z. Jiang, Z. Zhang, B. Han, Zn-N_x sites on N-doped carbon for aerobic oxidative cleavage and esterification of C(CO)-C bonds, Nat Commun, 2021, **12**, 4823.
6. Z. Dong, X. Yang, Q. Pan, Y. Ao, J. Du, M. Zhai, L. Zhao, Performance and mechanism of selective adsorption of silver to L-cysteine functionalized cellulose microsphere, Cellulose, 2020, 27, 3249–3261.